An Ultraviolet Study of Star-Forming Regions in M31

Yongbeom Kang[1,2], Luciana Bianchi[2,3], and Soo-Chang Rey[1,3]

[1]Department of Astronomy and Space Science, Chungnam National University, Daejeon, 305-764, Korea; ybkang@cnu.ac.kr, screy@cnu.ac.kr

[2]Department of Physics and Astronomy, Johns Hopkins University, Baltimore, MD 21218, USA; bianchi@pha.jhu.edu

[3]Corresponding authors

ABSTRACT

We present a comprehensive study of star-forming (SF) regions in the nearest large spiral galaxy M31. We use $GALEX$ far-UV (1344-1786 Å, FUV) and near-UV (1771-2831 Å, NUV) imaging to detect young massive stars and trace the recent star formation across the galaxy. The FUV and NUV flux measurements of the SF regions, combined with ground-based data for estimating the reddening by interstellar dust from the massive stars they contain, are used to derive their ages and masses. The $GALEX$ imaging, combining deep sensitivity and entire coverage of the galaxy, provides a complete picture of the recent star formation in M31 and its variation with environment throughout the galaxy. The FUV and NUV measurements are sensitive to stellar populations younger than a few hundred Myrs. We detected 894 SF regions, with size $\geq$ 1600 pc^2 above an average FUV flux limit of $\sim$26 ABmag arcsecond^{-2}, over the whole 26 kpc (radius) galaxy disk. We derive the star-formation history of M31 within this time span. The star formation rate (SFR) from the youngest UV sources (age $\leq$ 10 Myr) is comparable to that derived from Hα, as expected. We show the dependence of the results on the assumed metallicity. When star formation detected from IR measurements of the heated dust is added to the UV-measured star formation (from the unobscured populations) in the recent few Myrs , we find the SFR has slightly decreased in recent epochs, with a possible peak between 10 and 100 Myrs, and an average value of SFR $\sim$0.6 or 0.7 M$_\odot$ yr^{-1} (for metallicity Z=0.02 or 0.05 respectively) over the last 400 Myrs.

Subject headings: stars: early-type — galaxies: evolution — galaxies: individual (M31) — galaxies: star clusters — galaxies: structure — ultraviolet: galaxies — ultraviolet: stars

1. Introduction

In the cold dark matter framework, large spiral galaxies are built hierachically, and there is much observational evidence of galaxy interactions to support this. However, we still face many challenges in understanding the details of galaxy evolution. In this regard, it is interesting to study the hot, massive stellar populations in nearby galaxies which can be a robust tracer of recent star formation activity due to their short lives. Young massive stars contribute to the global characteristics at the current epoch of their host galaxy and play a major role in the galaxy evolution.

Young massive stars emit powerful ultraviolet (UV) radiation, therefore UV imaging is ideal to detect and characterize these stars, which are confused with older stellar populations in observations at longer wavelengths (Bianchi 2007, and references therein). In most cases, young massive stars are formed in associations in the galactic disk. We define these stellar associations from UV imaging, in order to study the spatial structure and intensity of the recent star formation. *Galaxy Evolution Explorer* (*GALEX*, Martin et al. 2005) imaging in far-UV (FUV) and near-UV (NUV) passbands is particularly useful to study massive stellar populations. Specifically, the integrated $FUV - NUV$ color of young stellar populations is very sensitive to the age of the population, owing to the rapid evolution of the most massive stars (e.g. Bianchi 2007, 2009: Fig. 9). Consequently, UV imaging data allow us to unambiguously identify the young stellar populations and to estimate their ages and masses from colors and extinction-corrected UV luminosities, respectively. These results provide the means of probing the history and modality of recent star formation in galaxies.

M31 is one of the two largest spiral galaxies in the Local Group, along with the Milky Way. However, there has been growing evidence that the Milky Way and M31 have different properties (Ibata et al. 2007, and references therein). M31 shows a lower star formation rate (SFR) than the Milky Way (Kennicutt 1998; Massey et al. 2007; Hou et al. 2008; Fuchs et

al. 2009). Furthermore, there are suggestions that M31 appears to be a more typical spiral galaxy than the Milky Way (Hammer et al. 2007). As with the bulk of local spirals, M31 shows evidences for a formation and evolution history affected by merging and/or accretion events, including substructures in its halo (Hammer et al. 2007, and references therein). In this respect, it is important to investigate the star-forming (SF) regions in M31. We present the first extensive study of the young stellar populations from UV imaging, covering the entire M31 disk within 26 kpc radius, and extending beyond this radius in some fields. By studying the SF regions in M31 traced by UV imaging, we investigate the recent star formation history of this galaxy.

In section 2, we describe the *GALEX* UV data used. We describe the detection and photometry of SF regions, from UV imaging, in section 3, and estimate their interstellar extinction in section 4. In section 5, we select OB associations from ground-based photometry of stellar sources and compare them with our UV-defined SF regions. The age and mass of the SF regions are derived in section 6, the star formation history in section 7, and the conclusions are presented in section 8.

2. Data

We focus on the disk region of M31 where most of the recent SF regions are located. We adopt the disk semi-major axis value of R = 26 kpc from Walterbos & Kennicutt (1988). We considered 20 fields from the *GALEX* fourth data release (GR4). *GALEX* observed the disk region of M31 as part of the Nearby Galaxies Survey (NGS, Bianchi et al. 2003). We rejected the fields which have only FUV observations and exposure time shorter than 2,000 s (except for "PS_M31_MOS03"), then selected the fields closer to the major axis when different pointings are located along the galaxy's major axis. The "PS_M31_MOS03" field has a shorter exposure than 2,000 s but it is the only *GALEX* field observed in the

south outermost disk region of M31. As a result, we selected 7 *GALEX* fields covering the entire disk region (see Fig. 1 and Table 1). Each selected *GALEX* field has FUV (1344-1786 Å) and NUV (1771-2831 Å) imaging with the same exposure time. *GALEX* FUV and NUV imaging has 4.2 and 5.3 arcsec resolution (FWHM) or about ∼19 pc in M31, and the field of view (FOV) is about 1.27 and 1.25 degree respectively (Morrissey et al. 2007). We used in our analysis only the central 1.1 degree diameter portion of the field, for best photometry. *GALEX* images have a sampling of 1.5 arcsec pixel^{-1} which corresponds to 5.67 pc, assuming a distance of 785 kpc (McConnachie et al. 2005).

3.   Photometry of Star-Forming Regions

The FUV images provide a direct measure of the flux from young massive stars not heavily embedded in interstellar dust. Most SF regions are gravitationally unbound systems and have irregular shapes. Rather than using aperture photometry, we constructed contours of the SF regions to trace their morphology, and measure their UV flux and flux density. The procedure was originally developed by Tolea (2009) in his dissertation, and we have modified the procedure for a more precise detection and photometry of the SF regions. Our procedure consisted of three steps. The first step was to detect all image pixels which have flux above a certain threshold in each FUV image. An important factor in detecting and defining SF regions is the brightness limit. The second step was to define the contours of each SF region from contiguous pixels detected above the threshold over a minimum area. In this way, we can define contours of SF regions even if they have a complicated shape, and reject isolated stars which are smaller than the minimum size. The third step was to estimate the background and to measure the flux of the defined SF regions. Even though the background in the UV image is much lower than in the optical, it is important to correctly subtract its contribution from the source photometry. We performed various

tests for determining the optimum flux threshold, minimum size of a SF region, and best background subtraction method.

We used the field "NGA_M31_MOS0" which has the longest exposure time (6,811 s) in our selected *GALEX* data, to test and refine our procedures, which were then applied to all our selected fields. This field is good for testing various types of SF regions because it contains portions from innermost to outermost spiral arms and the large OB association NGC 206. First of all, we compared various thresholds for the detection of source pixels. We used the background-subtracted image ("-intbgsub") provided by the GR4 pipeline. We estimated the mean background value by the sigma clipping method. We examined the results using thresholds of two, three, and five sigma above the mean background value (see Fig. 2). We detect fainter objects if we use the lower thresholds, however the SF regions in the spiral arms merge together and the contamination by the background (including older, diffuse populations) is larger. We can easily define the bright regions if we use higher thresholds, however we cannot detect the faint ones. The FUV magnitude limits of our detected SF regions from each threshold are shown in Fig. 3, they are ~21.5 (low), ~21.0 (mid), and ~20.4 (high threshold) mag in the AB magnitude system. We adopted a threshold of three sigma above the mean background value, which showed in our analysis less contamination by background and marginally detects the faint regions. This results in an average FUV flux threshold of ~0.0032 c s^{-1} pixel^{-1}, or ~25.9 mag arcsec^{-2}. Then, we considered the minimum acceptable size of the SF regions, in order to eliminate contamination by background objects, artificial sources, foreground stars, and isolated bright stars in M31. We considered 3×FWHM of *GALEX* (~13 arcsec or ~8.5 pixels) to be the minimum diameter of a SF region, and therefore we adopted a requirement of a minimum of 50 contiguous pixels ($\sim1,600$ pc^2 or ~40 pc) for the smallest SF region. We contoured the contiguous pixels selected for measuring the defined regions and we estimated the center of each SF region by the mid-point of the maximum diameter of its contour.

These adopted threshold and minimum size of the SF regions, were then applied to all the selected fields. However, the exposure time differences among fields induces variation of the detection limit. Therefore, we compared the detection fraction in overlapping image regions, one by one, against the "NGA_M31_MOS0" field. We first tried a fixed threshold ($\sim$0.0032 c s^{-1} pixel^{-1}) for source detection in the "NGA_M31_MOS0" image. In this case, in images with shorter exposure time, sources were over-detected and included noise. A second method used a variable threshold of three sigma above the mean background value from each image. This produced similar contours in the overlapping regions. However, some sources in the shorter exposure time images were under-detected because the background has larger sigma values. Finally, we adopted the ratio between detected and un-detected pixels of overlapping regions. This case produced slight over-detection in the shorter exposure time images. Therefore, we used the last method, manually varying the thresholds in each field, such as to obtain similar detections in overlapping regions. The final selected FUV pixel maps are shown in Fig. 4. As a last step, we compared the detected SF regions within overlapping image portions by visual inspection to select a final catalog of unique sources. In the end, we obtained a catalog of 894 SF regions cleaned of artifacts, isolated stars, and overlapping objects.

We measured the flux within the contours of the SF regions as defined above, and subtracted the local background, estimated in a circular annulus surrounding the source. We initially used an inner/outer size of the annulus of 1.5/3 times the size of each SF region. However, for the largest sources, which are mostly found along the spiral arms, the annulus for background measurement scaled in this way becomes too large and includes unrelated stellar populations. Therefore, we tested three different procedures to estimate the background. One was to measure the local background ("Ap. sky" in Fig. 5), adjusting the radius of the background annulus according to the size of the source. We adopted a variable scaling of inner/outer radii for the background annulus, adjusted as 2/4, 2/3,

1.5/2.5, 1.1/1.3, and 1.05/1.2 times the source size (R_{MAX}) for the following ranges of source size respectively: $R_{MAX} < 10$, $10 \leq R_{MAX} < 20$, $20 \leq R_{MAX} < 50$, $50 \leq R_{MAX} < 100$, and $100 \leq R_{MAX}$ ([pixels]). Such ranges were found adequate to ensure a large enough area for the background measurement for the smallest sources, while preventing excessively large areas to be included in the calculations for large sources. The second background estimate was obtained from the GR4 pipeline background image ("-skybg") , and the third measurement was performed by applying a median filter to the image. In the case of the GR4 pipeline background ("Pipe. sky" in Fig. 5), a sky background image is produced by a 5×5 median filter size which is good for the case of Poisson distribution (Morrissey et al. 2007). The background measured using this image, underestimates the local contribution by the galaxy's background light, especially from surrounding stellar populations in the spiral arms. In the case of the median filtered background ("Med. sky" in Fig. 5), a smaller filter size (3×3 pixels) than the standard pipeline was used to produce the background images. The choice of a smaller filter size was driven by the consideration of spiral arm regions which host most of the SF regions. The results from this background estimate are similar to those from the local background and reflect well the brightness of spiral arms. The results from the three methods are compared in Fig. 5. The background from the pipeline 'sky' image is always underestimated because it measures the lowest sky level and not the local diffuse stellar population surrounding the source. In the right-side panels in Fig. 5, we see that this estimate is not sensitive to the spiral arm enhancements, as the local-background estimates are. The local sky estimate is similar to the results from the median-filtered measurements but shows less scatter for sources with multiple observations in overlapping regions. In Fig. 6, we compare the photometry results using the three different methods for background subtraction in color-magnitude diagrams. Most SF regions have FUV − NUV color between −0.5 and 1.0 in ABmag. The measurements from the pipeline and median-filtered backgrounds induce brighter NUV than FUV, especially

for sources fainter than 20 mag. We finally adopted the result from the local background. The resulting catalog of SF regions and their *GALEX* photometry is given in Table 2.

4.   OB Stars and Interstellar Extinction

In order to derive the physical parameters of the SF regions from the integrated photometry, we must take into account the interstellar extinction. We estimated the reddening of each UV SF region from the reddening of the massive stars included within its contour. For massive stars we used the reddening-free parameter Q (Massey et al. 1995; Bianchi & Efremova 2006). We used the optical point-source measurements of M31 sources from Massey (priv. comm.), which is a revised M31 catalog from the NOAO survey data described by Massey et al. (2006, 2007). We selected sources with UBV measurements having photometric errors lower than 0.1 mag in all bands (108,089 objects out of their 371,781 total sources catalog), which results in a magnitude limit of about 23rd mag in V-band. This data is deep enough to select OB type stars which we could use to estimate the interstellar reddening of our SF regions. We selected OB type stars by comparing colors and brightness of the Galactic OB type main sequence stars from Aller et al. (1982). We selected stars from O3 to B2V, because a B2V star has $M_V = -2.45$ which is $V = 22.02$ in M31 ($m - M = 24.47$) in absence of extinction. We don't know the internal reddening of M31 a priori, therefore we used the reddening-free parameter Q_{UBV} to select the OB stars.

$$Q_{UBV} = (U - B) - \frac{E(U-B)}{E(B-V)}(B - V)$$

The $E(U - B)/E(B - V)$ ratio is a constant (0.72) for Milky Way dust type (Massey et al. 1995) and does not vary much for other dust types, within a reasonably small range of $E(B - V)$ (e.g. Bianchi et al. 2007; Bianchi & Efremova 2006, and references therein). We selected the OB stars which have Q_{UBV} between -0.97 (O3V) and -0.67 (B2V). In order

to reduce contamination, we also adopted magnitude and color limits; $-6.0 \leq M_V \leq -0.28$, $-0.34 \leq B - V \leq 0.46$, and $-1.22 \leq U - B \leq -0.336$ (Aller et al. 1982). The color and magnitude limits were derived assuming a maximum reddening value of $E(B - V) \leq 0.7$. The location of the selected OB stars in color-magnitude diagrams is presented in Fig. 7. With these restrictions, we finally selected 22,655 O-B2 stars from the data of Massey et al. (2006). The spatial distribution of these stars, shown in Fig. 1, represents well the spiral structure of M31.

The interstellar extinction of the selected OB stars was estimated from the reddening free parameter Q_{UBV}, using the empirical relationship for giant and main-sequence stars by Massey et al. (1995).

$$(B - V)_0 = -0.013 + 0.325 Q_{UBV} = (B - V) - E(B - V)$$

The estimated $E(B - V)$ has mean, median, and mode value of about 0.34, 0.32, and 0.29, respectively, from our selected OB stars. The mean reddening value of OB stars is larger than Massey et al. (2007)'s typical value $E(B - V) = 0.13$ which is estimated visually from the location of the "blue plume" in the color-magnitude diagram. This difference may be caused by our selection of blue stars for the reddening estimate. We also explore in this paper more reddened regions than the average entire stellar population. We estimated the extinction by interstellar dust for each SF region from the average reddening of the OB stars within the SF region contour. For the SF regions outside of Massey et al. (2006) survey, we assumed $E(B - V) = 0.20$. The spatial distributions of estimated interstellar reddening of OB stars and SF regions are shown in Fig. 8. The interstellar extinction decreases from the inner disk region outwards. In particular, inner-most and south-west areas where we could not detect SF regions, have high interstellar extinction. We will return to this point in the next section. Our detection method is based on the FUV flux, which could vanish in high interstellar extinction regions.

5. OB Associations Defined from Stellar Photometry

For comparison with our FUV-defined SF regions, we also used a Path Linkage Criterion (PLC: Battinelli 1991) method (explored by Ivanov 1996, 1998; Magnier et al. 1993; Tolea 2009) to detect OB associations using O-B2 stars. We applied the PLC method varying the minimum number of stars (N_{min}) and maximum link distance (d_s) (see Fig. 9). The best choice of N_{min} and d_s was found to be $N_{min} = 5$ stars and $d_s = 10.4$ arcsec ($\sim$40 pc). Magnier et al. (1993) found 174 OB associations and estimated a total number of $\sim$420 associations in M31 from a similar method but different optical photometry. With this method, we found 650 OB associations in M31 from the O-B2 stars selected by us from Massey et al. (2006) photometry, which is $\sim$ 2 mag deeper than what Magnier et al. (1993) used. We compared these OB associations with the 894 SF regions selected from FUV imaging. They mostly overlap with the FUV-detected regions (see Fig. 10), however some of FUV-selected SF regions have a larger area than OB associations defined from stellar photometry, and some additional OB associations are found from stellar photometry in high interstellar extinction regions. The observation fields of Massey et al. (2006) cover a smaller area than our *GALEX* imaging, therefore we compared our results within 17 kpc de-projected distance (about 1 deg^2; dashed ellipse in Fig. 10) from the center of M31. The total area of the SF regions derived from the FUV contours (Section 3), and of the OB associations derived from stellar photometry (above), are 4.1 % and 3.5 % of the area of the 17 kpc disk, respectively. The numbers of O-B2 stars are 9094/11350 and 8670/11774 inside/outside of UV-defined SF regions and of OB associations respectively. The average projected density of OB stars in the associations is 0.017 and 0.018 stars arcsec^{-2} from UV-selected SF regions and OB associations selected from stellar photometry, respectively. The projected density of stars inside SF regions is about a factor of 20 higher than in general field. The comparison between the two methods is interesting, because the FUV-selected contours are more affected by interstellar reddening than the optical stellar photometry, on

the other hand optical bands are not as sensitive as the FUV is to the T_{eff} of the hottest stars (e.g. Bianchi 2007, and references therein). The similarity of the total number of OB stars detected inside young associations and in the field, by the two methods is remarkable. The slight difference in the estimated area of the associations may be due, at least partly, to the low ($\approx$5 arcsec) spatial resolution of the *GALEX* imaging.

6.   Ages and Masses of Star-Forming Region

We estimated the ages of the SF regions by comparing the measured (FUV − NUV) colour with synthetic Simple Stellar Population (SSP) models, reddened by the extinction amount estimated for each region. We explored effects of metallicity and dust type on the results (e.g. Bianchi 2007, 2009). We then estimated the masses of the SF regions from the reddening-corrected UV luminosity and the derived ages. We used two sets of SSP models, one from Bruzual & Charlot (2003) (BC03) and the other from the Padua group (PD: Bressan A., priv. comm.). The ages derived from the two grids of models do not differ significantly (see lower left panel of Fig. 11). Ages estimated using the BC03 models tend to be slightly younger than those derived using the PD models, below 30 Myrs, and do not differ at all for older populations (Fig. 11, lower left panel). The small age difference propagates to the derived masses, as shown in the lower-right panel of Fig. 11. The differences between results from the two model grids is not significant. We used the PD models in our analysis.

Most SF regions have UV colour between −0.5 and 1.0 (see upper left panel of Fig. 11). The estimated ages of most SF regions in our sample are younger than 400 Myrs, reflecting our FUV-based selection. Our detection limit, plotted with a line in the upper-right panel of Fig. 11, indicates quantitatively how the flux-detection limit translates into mass detection limit, as a function of age, and shows that we cannot detect low mass SF regions at older

ages, as expected. However, we also notice a lack of massive SF regions at younger ages. This will be discussed later.

We explored three metallicity values: subsolar (Z=0.008), solar (Z=0.02), and supersolar (Z=0.05) metallicity, although M31 is believed to have a typical metallicity about twice that of the MW (e.g. Massey 2003, and references therein). Our census of young stellar populations based on wide-field FUV imaging has an unprecedented extent, while direct metallicity measurements from spectroscopy are confined to limited samples. Therefore, we wanted to assess in general the dependence of our results on metallicity, which may vary in some environments. We also examined the effect of four types of interstellar dust: Milky Way ($R_V = 3.1$; MW, Cardelli et al. (1989)), average Large Magellanic Cloud (AvgLMC), 30 Doradus (LMC2) (Misselt et al. 1999), and Small Magellanic Cloud (SMC, Gordon & Clayton 1998) dust extinction. The resulting ages and masses of the SF regions are plotted in Figs 11, 12, and 13.

The differences in derived ages and masses for three metallicity values and different types of interstellar dust are presented in Fig. 12. We considered metallicity values of no less than Z=0.008 because we expect the young SF regions not to be as metal poor as old globular clusters. In Fig. 12 ages and masses derived from models with solar metallicity, and assuming MW-type interstellar reddening ($R_V = 3.1$), are compared to results from subsolar (Z=0.008) and supersolar (Z=0.05) metallicities (top four panels). The derived ages are older for subsolar metallicity, and younger for supersolar metallicity, with respect to solar metallicity results. The differences are most significant for ages younger than 100 Myrs (see also Fig. 9 of Bianchi 2009) and are up to a factor of ∼3 at most. Because the effect is stronger at certain ages, the number distribution of SF regions with ages also differs, as shown in Fig. 12. This will be taken into account in the following analysis, where we derive the global SF in M31 as a function of time. The difference in the derived masses

is not conspicuous, considering the uncertainties. The uncertainty of the ages derived by comparing the photometry to synthetic population models, reported in Table 2, is derived by propagating only the photometric errors, because we investigated and showed separately the effects of different metallicity values and dust types. The uncertainty on the derived masses reflects the uncertainty on the photometry and the age. Reddening corrections, as derived in Section 5, are applied.

The lower four panels of Fig. 12 show the effects of the correction for reddening. If the selective extinction by dust is steeper in the UV than the MW dust, as observed for example in the LMC (average) or the extreme starburst regions 30 Dor (labelled as "AvgLMC" and "LMC2", respectively, in Fig. 12), the dereddened UV luminosity will be higher but the dereddened $FUV - NUV$ color bluer, resulting in much younger ages and consequently lower masses. An LMC-type dust is however not likely in M31. Bianchi et al. (1996) report UV extinction curves in M31 similar to the average MW extinction, from UV spectra of OB stars. Moreover, if we apply UV extinction steeper than MW dust, most measured $FUV - NUV$ colors appear to be over-corrected, when compared to SSP model predictions. Out of 847 SF regions whose $(FUV - NUV)_0$ is within the model color range when dereddened with MW dust type, only 569/227/26 SF regions have $(FUV - NUV)_0$ colors within the model range if the progressively steeper dust types AvgLMC/LMC2/SMC are applied. Therefore, UV-steep dust extinction seems to be not realistic in most cases.

7. Results

7.1. Spatial distribution of the Star-Forming regions

The FUV-selected SF regions follow the disk structure of M31 and their spatial distribution traces the recent star formation in M31 (Fig. 13). As can be seen in Fig. 13,

most SF regions have de-projected distances between 40 and 75 arcmin (9 and 17 kpc) from the center of M31, with two peaks in this region. This region is well-known as the ring of fire or the star-formation ring (Block et al. 2006, and references therein). In this star formation ring between 40 and 75 arcmin from the galaxy center, the number of young ($<$ 10 Myrs) SF regions is similar to that of older ($>$ 10 Myrs) ones. One thing of interest is that the number of younger SF regions (82) is larger than the number of older SF regions (40) outside of this ring ($d_{de-projected} > 75$ arcmin). Inside of the star formation ring, the number of younger SF regions (14), however, is less than that of older ones (89). This suggests that the M31 disk formed stars continuously during the last few hundreds Myrs at least and, furthermore, the outer disk shows more recent star formation.

The size of some younger SF regions is larger than that of older SF regions, however most of them are less massive (as derived from the UV flux) than older regions. Young, large SF regions may be broken into several SF regions with time, while some of the dense, small SF regions may survive longer than the others.

7.2. Recent Star Formation History in M31

We noticed a lack of massive SF regions younger than 50 Myrs in Fig. 11. We would expect to find some massive young SF regions if star formation was constant. We estimated the total SFR in M31 using the ages and masses of the SF regions derived in Section 6. We added the estimated initial masses of the SF regions separated in four time bins, to investigate the SFR time evolution. The results are shown in Fig. 14, and reported in Table 3, for three metallicity values. Although in each age interval the derived SFR depends on the assumed metallicity, in all cases Fig.14 shows an apparent decrease of SFR in the recent epoch ($<$ 10 Myrs) with respect to the average value in the interval 10-100 Myrs ago, the difference being smallest (and probably not significant) for supersolar metallicity, which

is currently believed to be the most probable value for M31. The dashed line across the whole time interval is the average from the SF regions of all ages. When interpreting this diagram, we must first of all recall that the masses are estimated from the UV flux above a certain threshold, and the corresponding limit for mass detection increases at older ages (Fig. 11, continuous line). Therefore, the total stellar mass formed over 100 Myrs ago may be relatively underestimated compared to that of younger populations, due to our FUV selection. This bias makes the apparent decrease in SFR at young ages more robust. Most of the time-binned and mean SFRs are lower than one solar mass per year. These values can be compared to the M31's SFRs from IR and Hα. Barmby et al. (2006) estimated a SFR of 0.4 $M_\odot$ yr^{-1} from 8 μmm non-stellar emission, higher than our UV-derived SFR in the <4 Myrs bin, if we assume solar metallicity, but comparable to our value for supersolar metallicity. This shows that each indicator alone, UV or IR, may miss about half of the most recently formed stellar mass. Massey et al. (2007) estimated 0.05 $M_\odot$ yr^{-1} from Hα luminosities, lower (within a factor of two) than our estimate for the <10 Myrs bin (solar metallicity).

8. Conclusion and Discussion

We used 7 *GALEX* fields covering the entire disk of M31 (out to $\sim$ 26 kpc radius) to study its young stellar population. We detected 894 SF regions from the FUV imaging, and measured their integrated FUV and NUV fluxes. We estimated the interstellar extinction in each SF region from the OB stars within its contour, using the ground-based stellar photometry of Massey et al. (2006). We estimated ages and masses of our SF regions in M31, detected from FUV imaging, by comparing the FUV and NUV measurements to population synthesis models. Most are younger than 400 Myrs (UV is not sensitive to older ages). Interestingly, there are no massive SF regions at young ages (age < 50 Myrs in Fig.

11), suggesting an apparent decrease of the SFR, as detected from the FUV imaging.

There may be a potential bias, due to our definition of the SF contours from the FUV image, concerning the size distribution and average surface brightness. Younger SF complexes tend to be more compact, and older stellar associations are less dense, in general (Bianchi 2007; Efremova & Bianchi 2009). Therefore, the same flux detection algorithm may break a young SF area into several peaks, but these contiguous regions may appear connected if they spread out at older ages. This bias, however, does not appear significant from visual inspection of the complex SF areas along spiral arms, and younger associations tend to have larger size in our selection. In any case, the bias would only affect the apparent distribution [with age] of sizes and masses of the individual SF regions, and not affect the results when we add all individual masses in a wide age interval, in order to derive the total SFR in M31. Because we have estimated ages and masses of the individual SF complexes, and the UV flux is sensitive to a much broader age range than e.g. Hα or IR, we were also able to derive the recent SFR in M31 as a function of time. We estimated the SFR in four time intervals adding the masses of the SF regions of corresponding ages. The resulting masses are restricted by our detection limit which is shown in Fig. 11. The plot in Fig. 14 shows a recent apparent decrease of the SFR, as derived from the UV flux. However, we know that the youngest and compact SF regions are often still embedded in dust (e.g. Bianchi 2007, and references therein). These escape detection from UV imaging, but are instead revealed by IR emission from heated dust. Therefore, for a complete account of star formation in the very young age bins ($<$ 10 Myrs), we added the IR-measured star formation from Barmby et al. (2006). The total SFR at young ages (UV + IR estimates) is shown as thick lines at the top of vertical arrows in Fig. 14. This more realistic and complete estimate of the star formation in the recent few million years significantly reduces the apparent recent decrease in SFR, as derived from UV flux only.

We also show the average stellar mass formed in a $\leq$ 10 Myrs bin, from our UV measurements, for comparison to Hα estimates. Because Hα is an indirect measurement of the ionizing photons from the short-lived O-type stars, the SFR derived from this method must be compared to our age bin of $\leq$ 10 Myrs. The UV and Hα SFR estimates agree within a factor of two, for solar metallicity, as shown in Fig. 14. If we assume supersolar metallicity for all sources (Z=0.05), then the Hα underestimates the SFR by a factor of ten with respect to the SFR derived from the UV sources in the recent 10 Myrs. We note that the results shown in Fig. 14 are derived by dereddening the UV fluxes with MW-type dust extinction. If UV-steeper reddening applies to the intrinsic dust extinction in some SF regions, their derived ages would be younger (see Fig. 12), resulting in a SFR lower for older ages and higher for younger ages than the values shown in Fig.14, and increasing the discreapancy with the Hα estimate.

Even when the IR- and UV-derived SFRs are added at the youngest epochs, there seem to be a recent decrease of SFR, or a peak of SFR between $\sim$ 10-100 Myrs (although the UV estimate of SF at older ages is a lower limit, as previously explained). This seems to suggest that M31 had a starburst during this interval. A possible scenario is that galaxy interaction may have induced violent star formation around this time interval. Gordon et al. (2006) considered a collisional event with M32 around 20 Myrs ago to explain the ring structure by dynamical models. Block et al. (2006) also postulated a head-on collision event with M32 and estimated it happened around 210 Myrs ago. We now have a possible evidence of a recent starburst in M31, which may have constructed the ring structure.

This work presented the first estimate of the recent SFR based on measurements of individual SF regions across the entire galaxy, from UV imaging. Massey et al. (2007) provide a comparison of SF, based on Hα measurements, among Local Group galaxies, and several other authors give estimates of SF in nearby galaxies. However, their results

are mostly derived under the assumption of continuous star formation, translating global fluxes into SF. Our study provides a time-resolved SFR over the past few hundred million years. We will perform a similar analysis on other Local Group galaxies, for a consistent comparison of results from our method within a range of physical environments. Such comparison should also clarify the relative calibration of UV, IR, and Hα as SF indicators as a function of galaxy physical conditions.

In future works, we will also compare the parameters describing the properties of SF regions from the integrated measurements with resolved studies of their stellar populations (from ground-based and Bianchi's HST programs data). We will estimate ages and masses from deeper *GALEX* images to test the limit of our current detection threshold.

REFERENCES

Aller, L. H., et al. 1982, Landolt-Bornstein: Numerical Data and Functional Relationships in Science and Technology

Barmby, P., et al. 2006, ApJ, 650, L45

Battinelli, P. 1991, A&A, 244, 69

Bianchi, L. 2007, in UV Astronomy: Stars from Birth to Death, ed. A. Gomez de Castro & M. Barstow, 65

Bianchi, L. 2009, Ap&SS, 320, 11

Bianchi, L., & Efremova, B. V. 2006, AJ, 132, 378

Bianchi, L., Clayton, G. C., Bohlin, R. C., Hutchings, J. B., & Massey, P. 1996, ApJ, 471, 203

Bianchi, L., Madore, B., Thilker, D., Gil de Paz, A., Martin, C., & The GALEX Team 2003, The Local Group as an Astrophysical Laboratory, 10

Bianchi, L., et al. 2007, ApJS, 173, 659

Block, D. L., et al. 2006, Nature, 443, 832

Bruzual, G., & Charlot, S. 2003, MNRAS, 344, 1000

Cardelli, J. A., Clayton, G. C., & Mathis, J. S. 1989, ApJ, 345, 245

Efremova, B. V. & Bianchi, L. 2009, in preparation

Fuchs, B., Jahreiß, H., & Flynn, C. 2009, AJ, 137, 266

Gordon, K. D., & Clayton, G. C. 1998, ApJ, 500, 816

Gordon, K. D., et al. 2006, ApJ, 638, L87

Hammer, F., Puech, M., Chemin, L., Flores, H., & Lehnert, M. D. 2007, ApJ, 662, 322

Hou, J. L., Yin, J., Boissier, S., Prantzos, N., Chang, R. X., & Chen, L. 2008, arXiv:0807.2492

Ibata, R., Martin, N. F., Irwin, M., Chapman, S., Ferguson, A. M. N., Lewis, G. F., & McConnachie, A. W. 2007, ApJ, 671, 1591

Ivanov, G. R. 1996, A&A, 305, 708

——. 1998, A&A, 337, 39

Kennicutt, R. C., Jr. 1998, ApJ, 498, 541

Magnier, E. A., et al. 1993, A&A, 278, 36

Martin, D. C., et al. 2005, ApJ, 619, L1

Massey, P. 2003, ARA&A, 41, 15

Massey, P., Armandroff, T. E., Pyke, R., Patel, K., & Wilson, C. D. 1995, AJ, 110, 2715

Massey, P., Olsen, K. A. G., Hodge, P. W., Strong, S. B., Jacoby, G. H., Schlingman, W., & Smith, R. C. 2006, AJ, 131, 2478

Massey, P., Olsen, K. A. G., Hodge, P. W., Jacoby, G. H., McNeill, R. T., Smith, R. C., & Strong, S. B. 2007, AJ, 133, 2393

McConnachie, A. W., Irwin, M. J., Ferguson, A. M. N., Ibata, R. A., Lewis, G. F., & Tanvir, N. 2005, MNRAS, 356, 979

Misselt, K. A., Clayton, G. C., & Gordon, K. D. 1999, ApJ, 515, 128

Morrissey, P., et al. 2007, ApJS, 173, 682

Tolea, A. C. 2009, Ph.D. Thesis

Walterbos, R. A. M., & Kennicutt, R. C., Jr. 1988, A&A, 198, 61

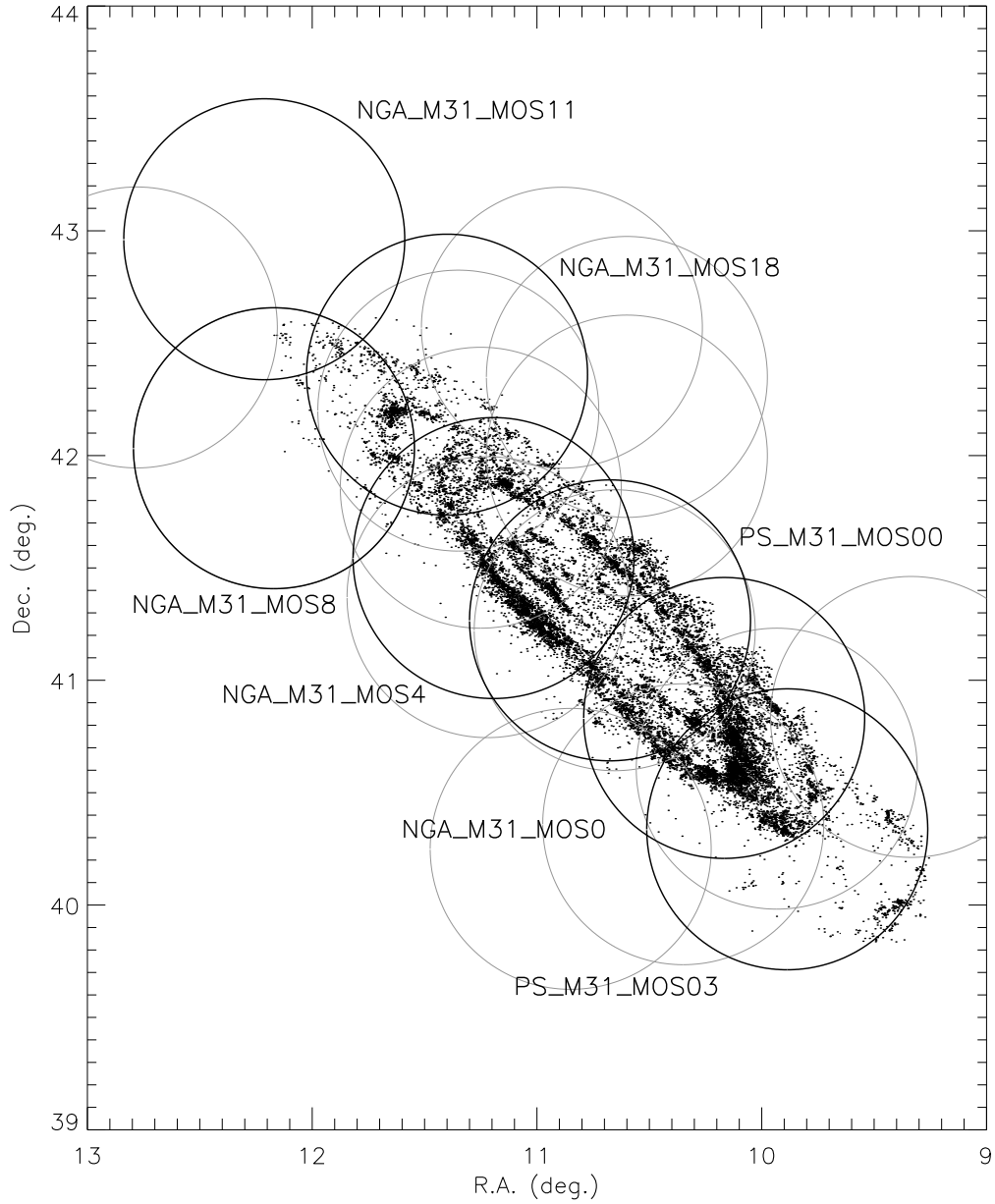This manuscript was prepared with the AAS LaTeX macros v5.2.

Fig. 1.— *GALEX* fields covering the M31 disk region from the GR4 data release. Black circles are our selected *GALEX* fields and grey circles are additional *GALEX* observations, not selected. Black dots are OB type stars selected from the ground-based photometric catalog of Massey et al. (2006), as described in Section 4.
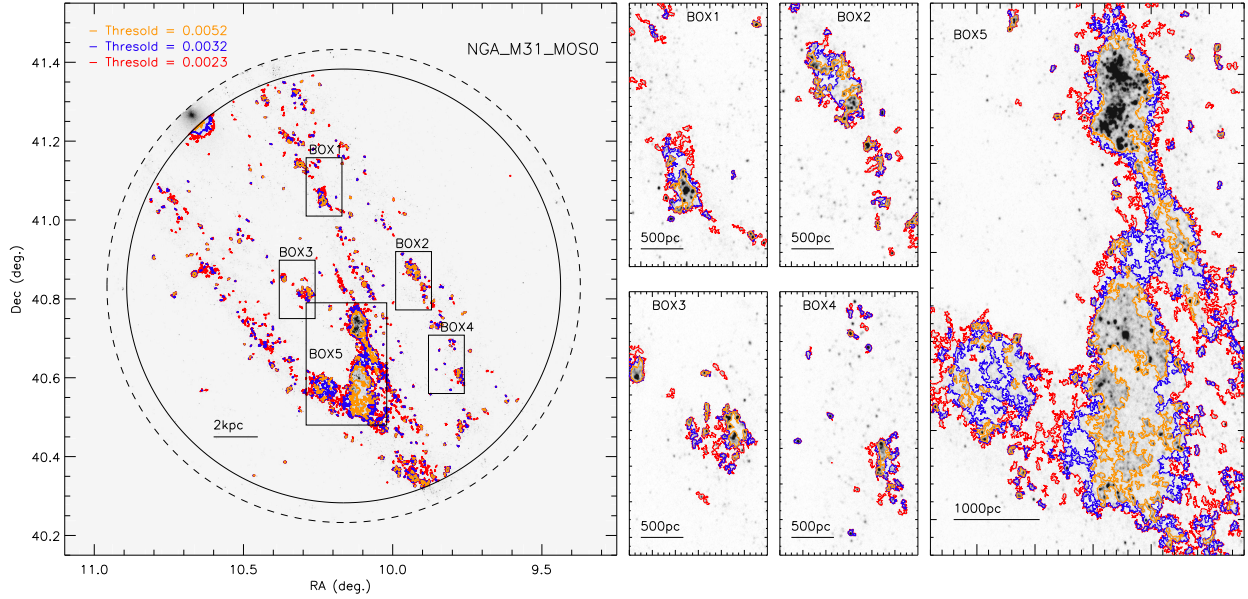
Fig. 2.— Differences of source detection in the "NGA_M31_MOS0" field using three different flux thresholds. Red contours are derived using the low threshold (mean background + 2σ), blue contours using the mid threshold (mean background + 3σ), and orange contours using the high threshold (mean background + 5σ). The solid circle is the FOV used in our analysis and the dashed circle is the whole *GALEX* FOV. Enlargements of sample regions are shown in the rectangular panels. Background images are the grey scaled FUV images of the "NGA_M31_MOS0" field.
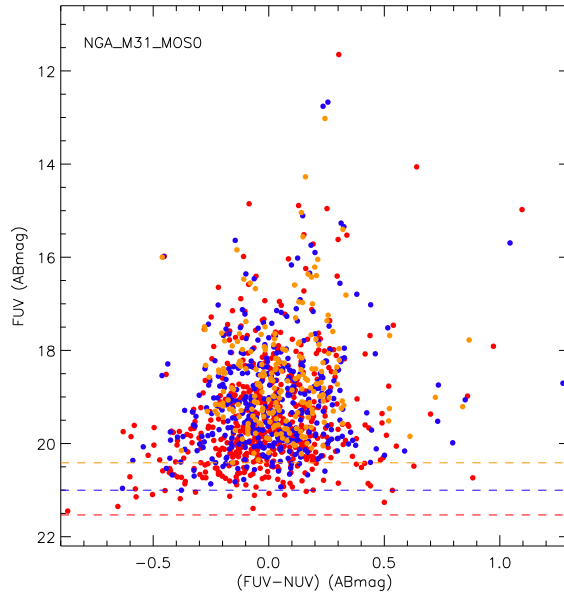
Fig. 3.— The color-magnitude diagram of SF regions in the "NGA_M31_MOS0" field. Red dots are detections using the low flux threshold (mean background + 2σ), blue dots are for the mid threshold (mean background + 3σ), and orange dots are for the high threshold (mean background + 5σ). Dashed lines are the magnitude limit of each threshold.
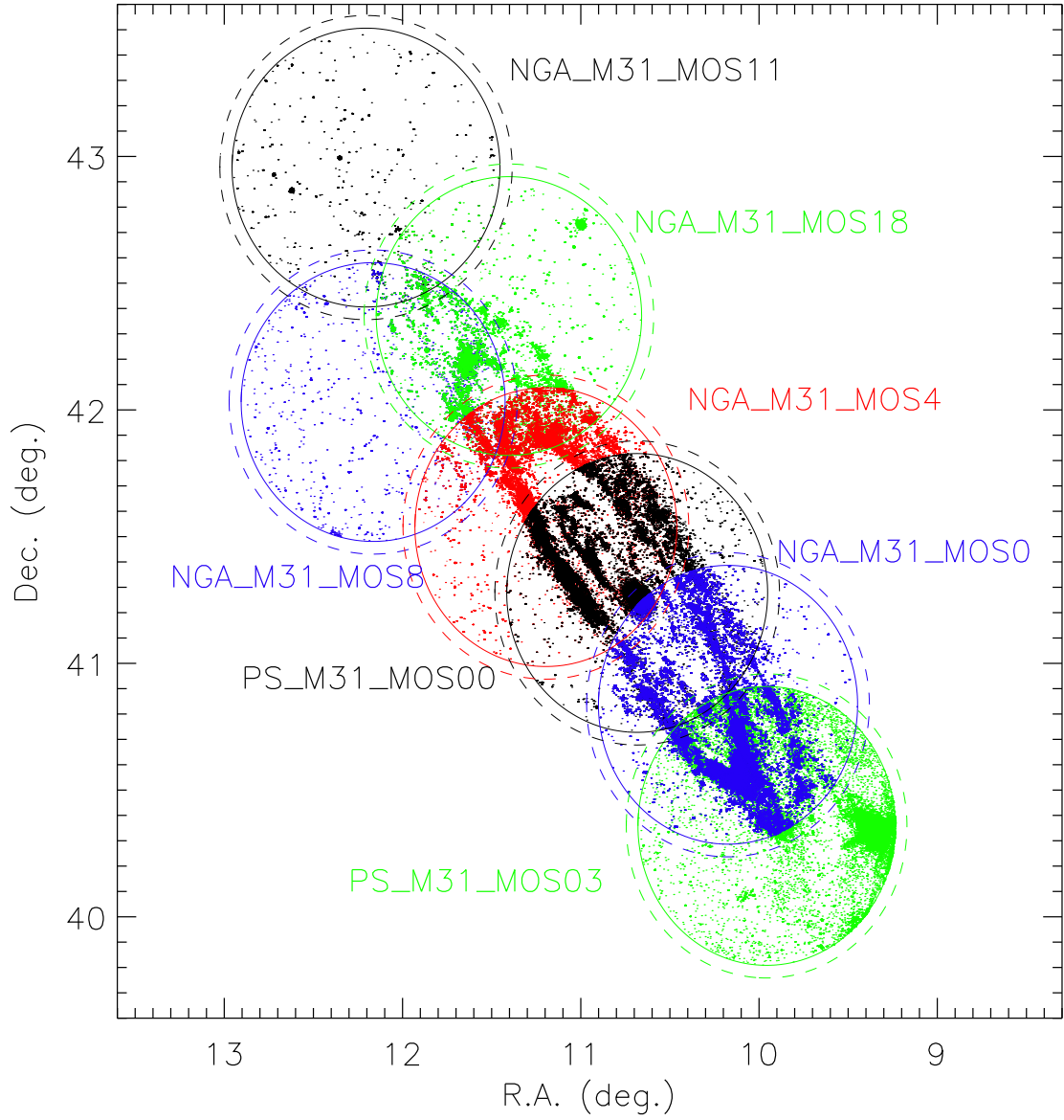
Fig. 4.— The detected FUV pixel map of the selected 7 *GALEX* fields. The solid circles are the FOV of our selection (1.1 degree diameter) and the dashed circles are the whole FOV of *GALEX*.
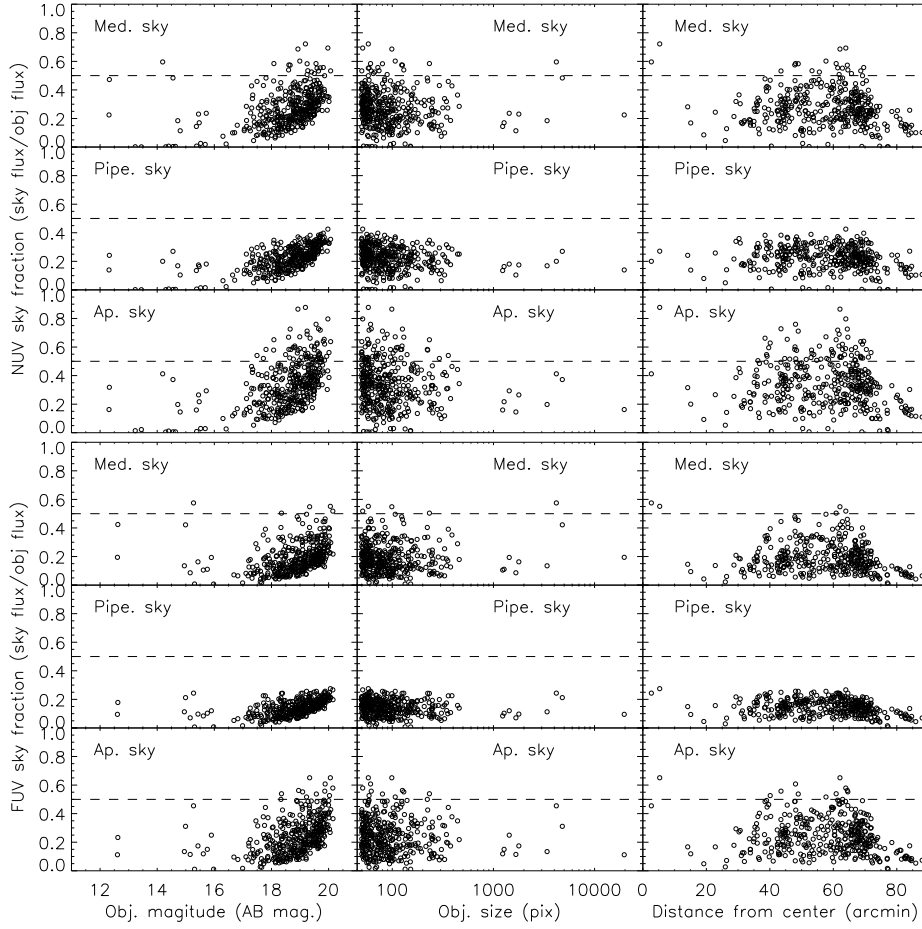
Fig. 5.— Comparison of three different methods of sky background estimations. The sky fraction in our photometry ("NGA_M31_MOS0" field) is displayed as the fraction of sky flux over object's original flux (sky un-subtracted flux). In the first and second column, it is plotted as a function of the measured magnitude of objects and the size of the objects, respectively. In the third column, it is plotted as a function of the de-projected distance from the center of M31. The upper 9 panels are NUV measurements and the lower 9 panels are FUV. The background is always higher in NUV because this filter includes light from older, more diffuse populations. Therefore, the background subtraction is more critical for NUV.
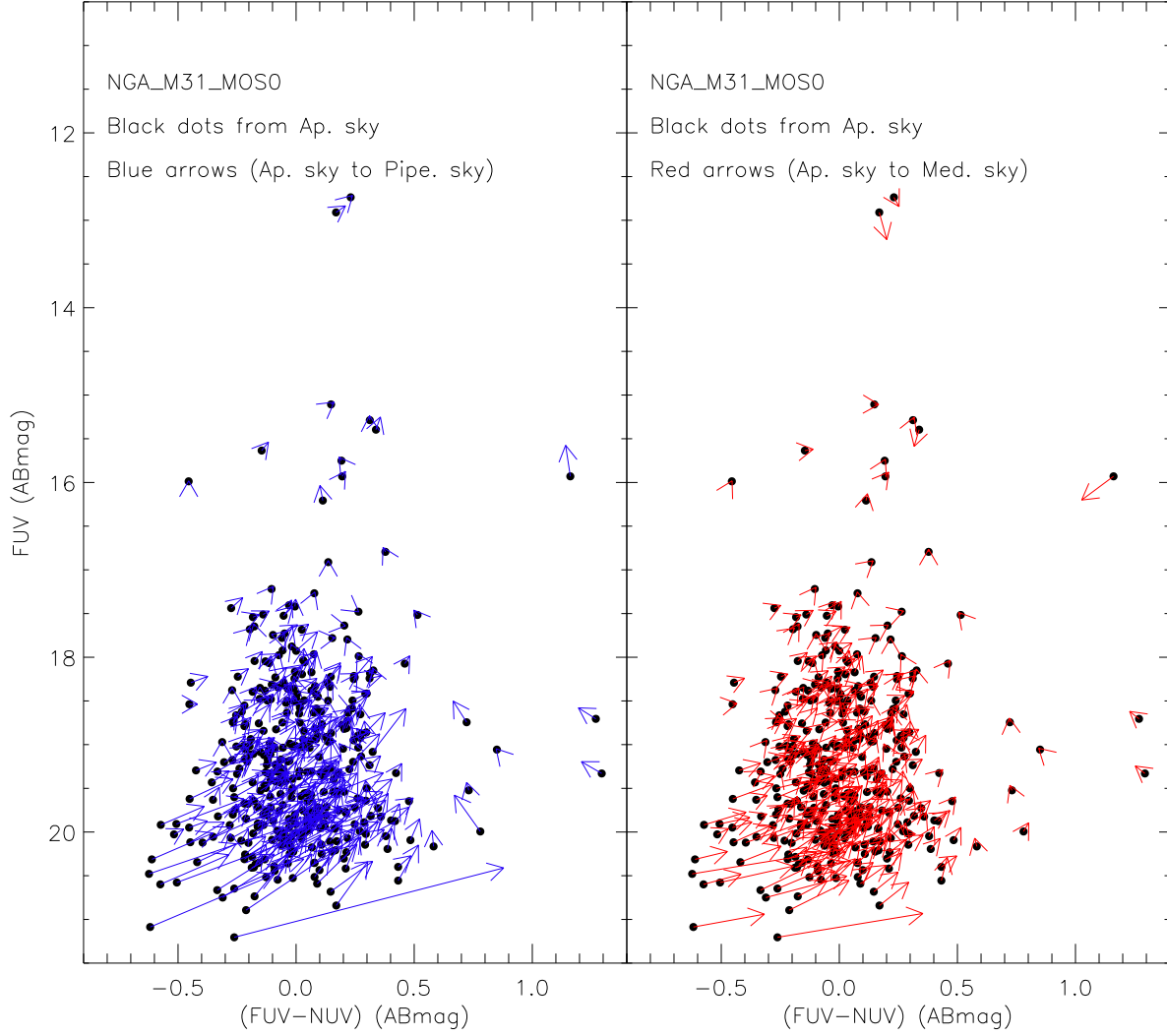
Fig. 6.— Comparison of photometry of the UV sources obtained from three different types of sky subtraction for the "NGA_M31_MOS0" field. Black dots are obtained subtracting the sky flux measured from the local background. The end points of the blue arrows (left panel) are the photometry results using the GR4 pipeline sky. The end points of the red arrows (right panel) are from our median (3×3 pixel) filtered sky.
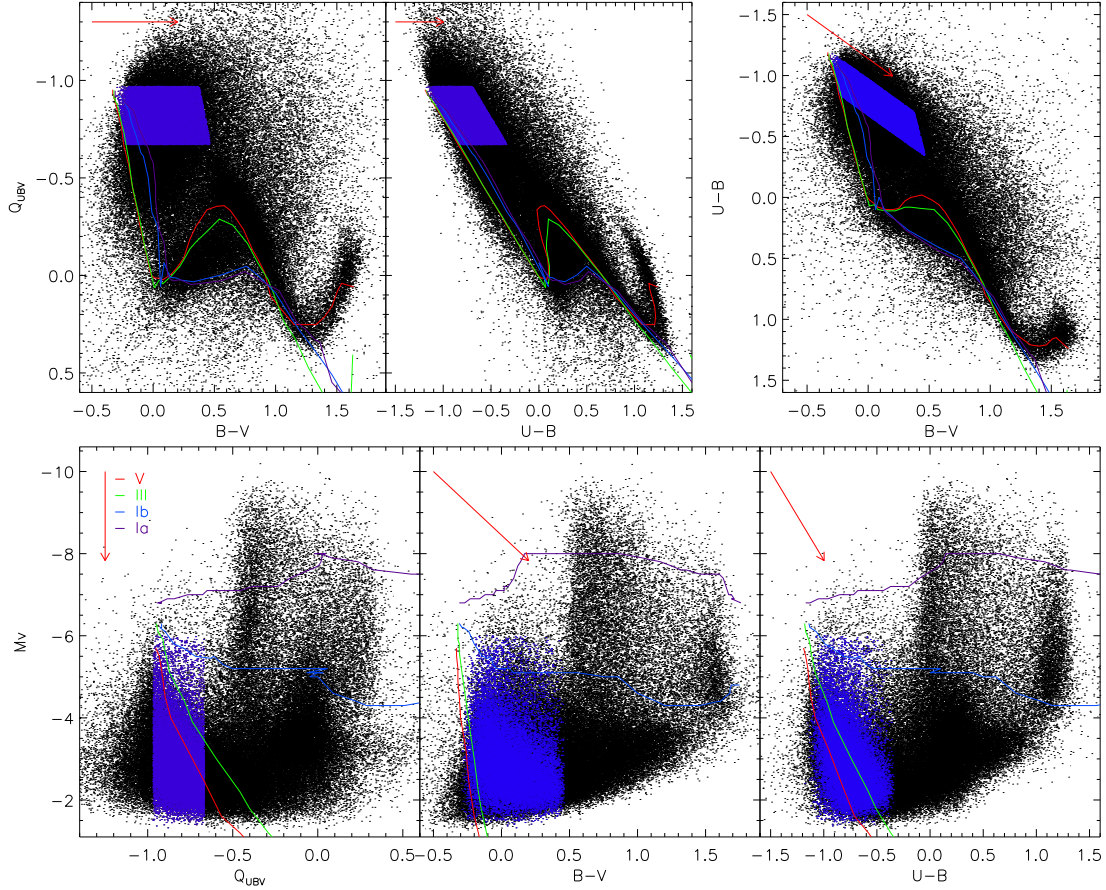
Fig. 7.— The selection of OB type stars from the ground-based photometry of Massey et al. (2006). The plotted points have magnitude error in UBV bands lower than 0.1 mag. Blue points are our selected OB stars. The lines represent the intrinsic color as a function of T_{eff} for luminosity classes main-sequence (V, red), giant (III, green), and supergiant (Ib and Ia, blue and purple) from Aller et al. (1982). The red arrow in each panel is the direction of reddening with $E(B - V) = 0.7$.
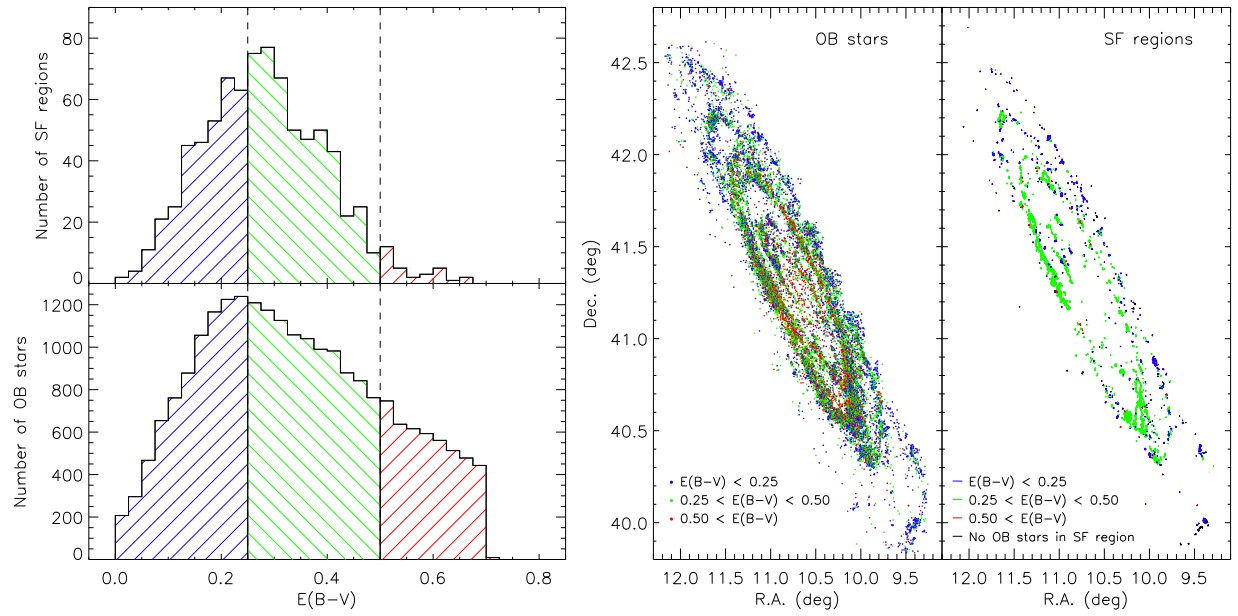
Fig. 8.— Number distributions of reddening for the selected OB stars and for the detected SF regions (left panels). Spatial distributions of OB stars and SF regions are presented color-coded by three ranges of reddening in the right panels.
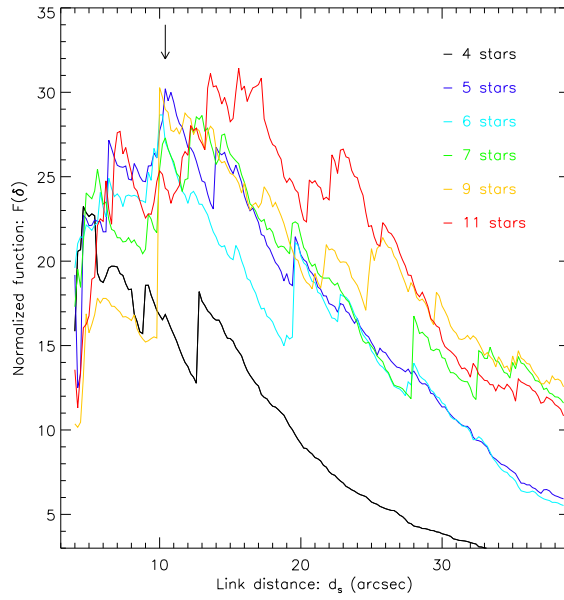
Fig. 9.— The mean normalized fluctuation function changes with the minimum number of stars of an association (N_{min}) and the maximum link distance (d_s) between stars. The black arrow indicates the maximum peak of this function, which defined the parameters adopted for our selection of OB associations.
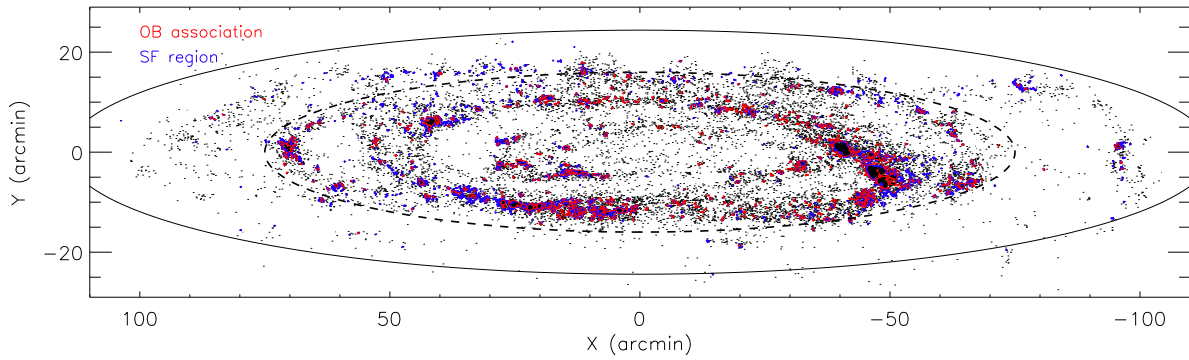
Fig. 10.— Spatial distribution of SF regions detected from the *GALEX* imaging (blue contours) and OB associations from optical stellar photometry (red contours). Black dots are the selected OB stars. The solid ellipse has a 26 kpc de-projected radius and the dashed ellipse has a 17 kpc de-projected radius.
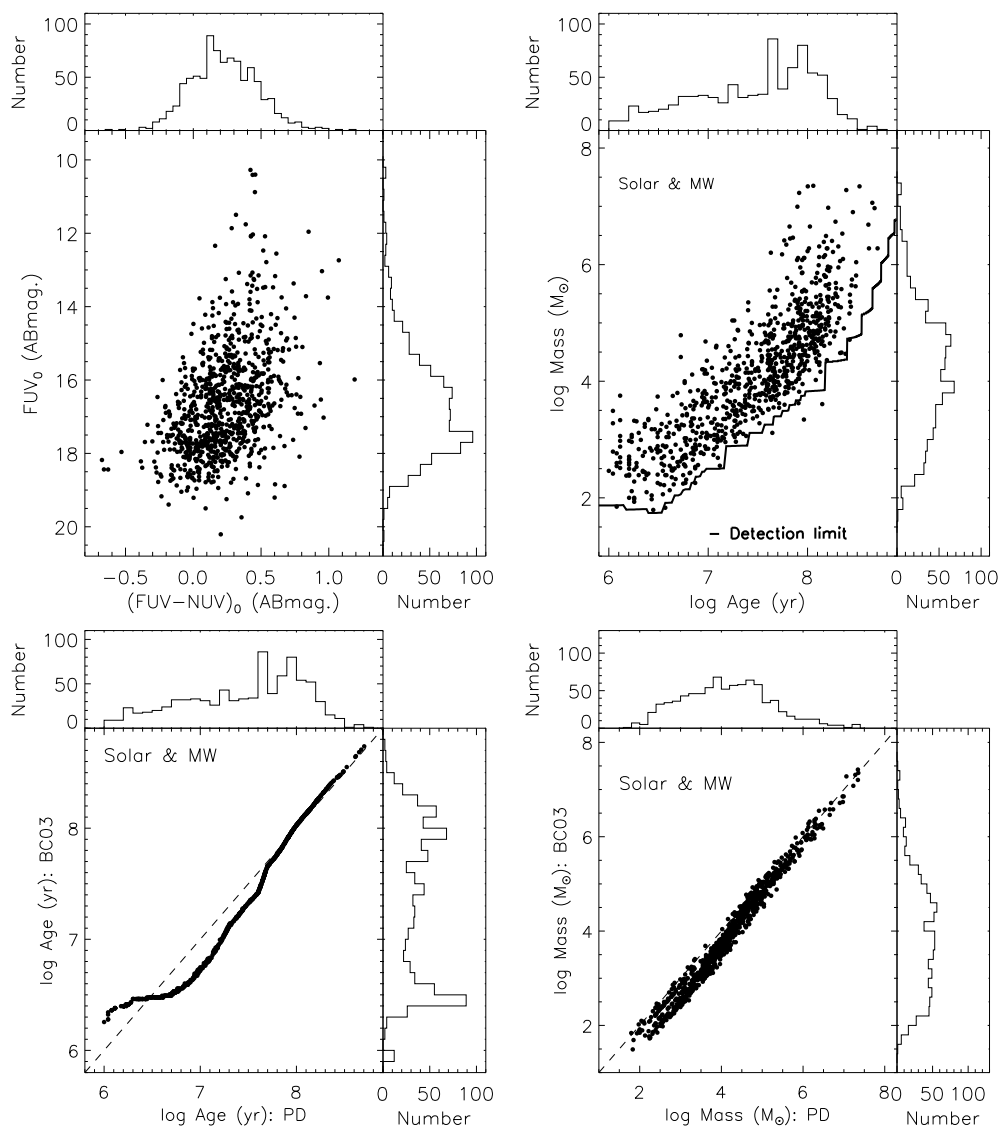
Fig. 11.— Upper left panel: the colour-magnitude diagram of the SF regions. Upper right panel: the estimated ages and masses assuming solar metallicity (Z=0.02) with interstellar extinction of MW dust type using the PD model grid. The line below the data points is the model-estimate of our detection limit, based on the limiting magnitudes. Lower left/right panels: age/mass differences between two sets of models, assuming solar metallicity with MW dust type.
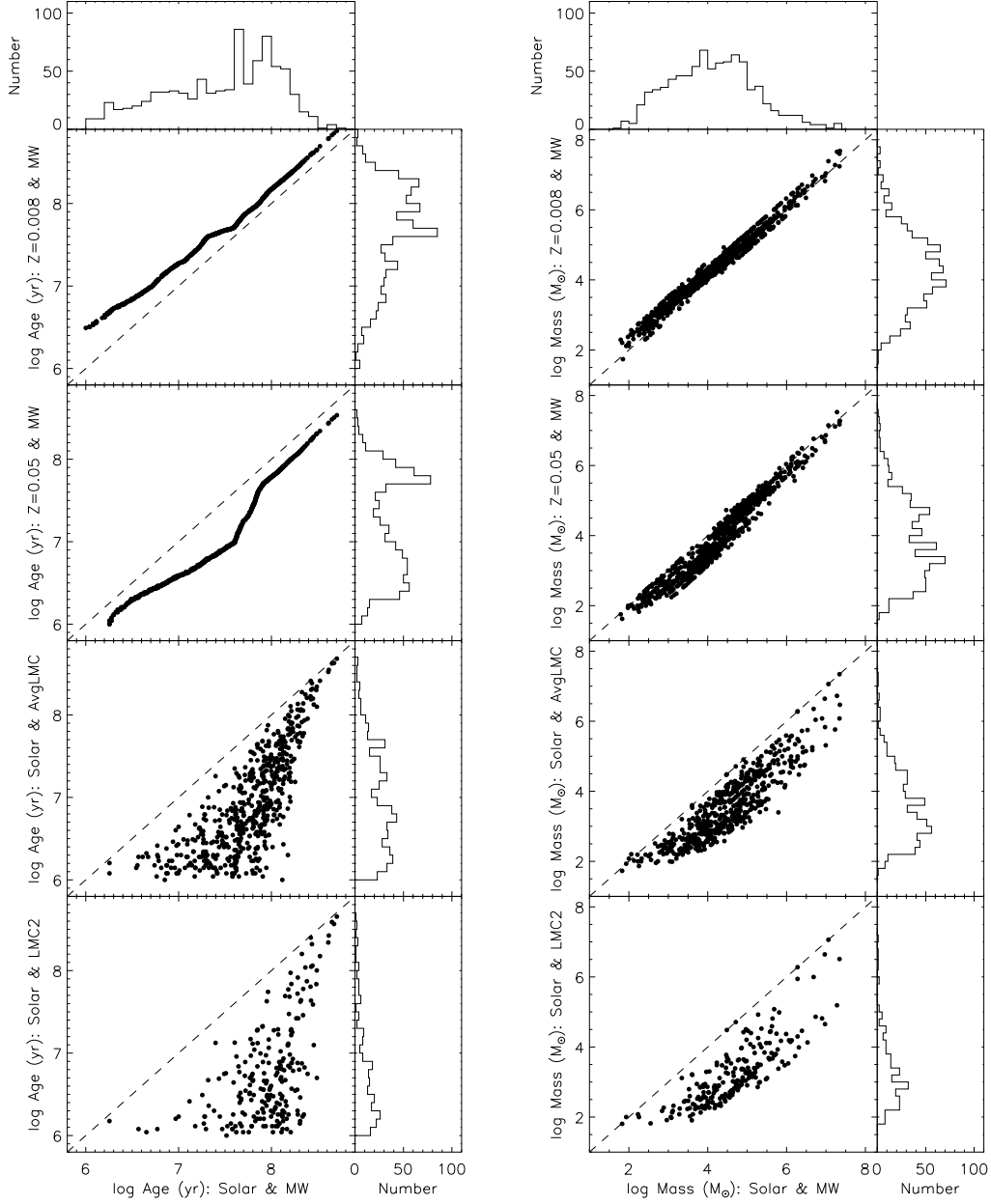
Fig. 12.— Ages and masses of the SF regions, derived assuming various metallicities and dust types. Results from the PD models are shown.
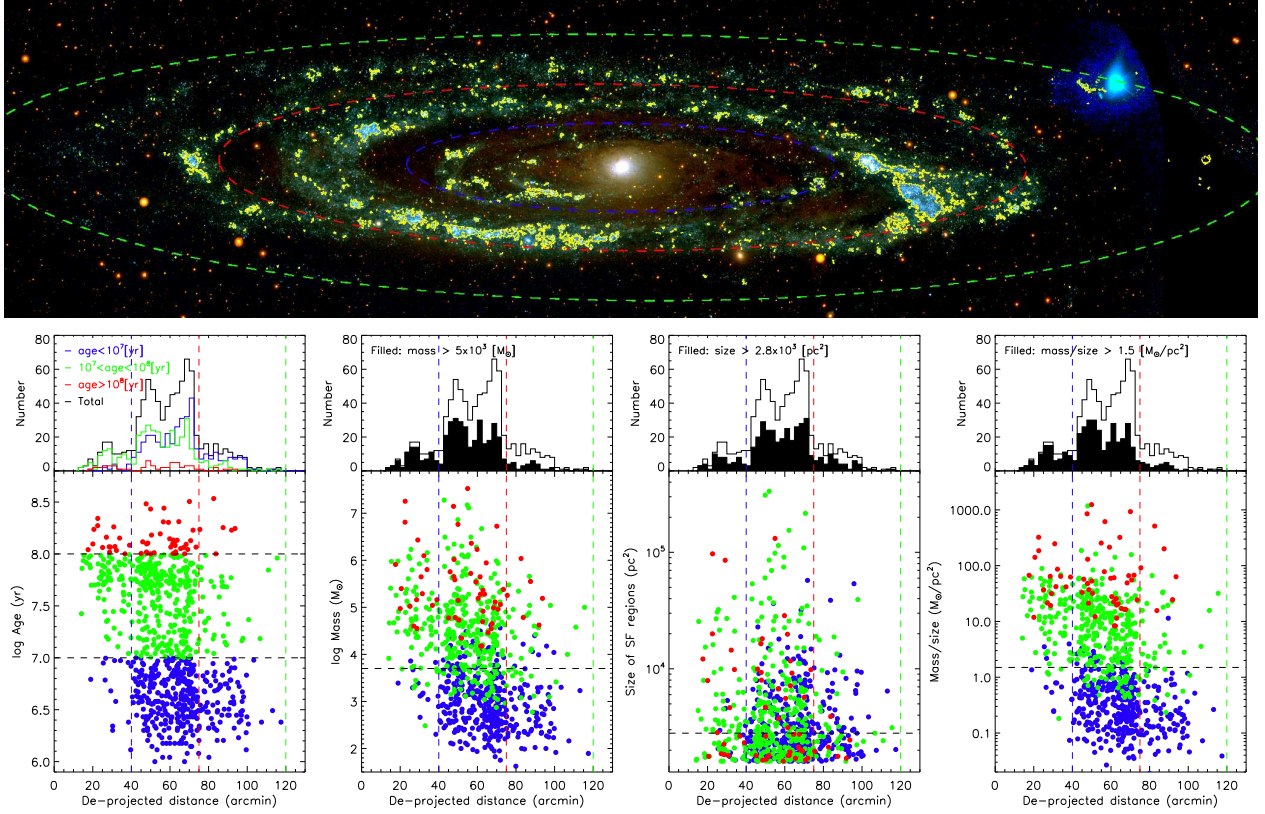
Fig. 13.— Top panel: the spatial distribution of SF regions (yellow contours) on a colour composite image (blue: FUV, green: FUV+NUV, red: NUV). The bright blue blob on the outermost ellipse is a bright Galactic foreground star (HD 3431). Bottom panels: distributions of ages, masses, size, and mass-per-unit-area of SF regions against the de-projected distance from the center of M31. Different symbol colors indicate different age bins (red: older than 100 Myrs, green: 10 - 100 Myrs, blue: younger than 10 Myrs). The dashed vertical lines correspond to the ellipses drawn on the top image at 40, 75, and 120 arcmin, corresponding to deprojected distances in M31 of 9, 17, and 27 kpc, respectively. The ages and masses shown here were derived using metallicity Z=0.05 and MW (R_V=3.1) dust type.
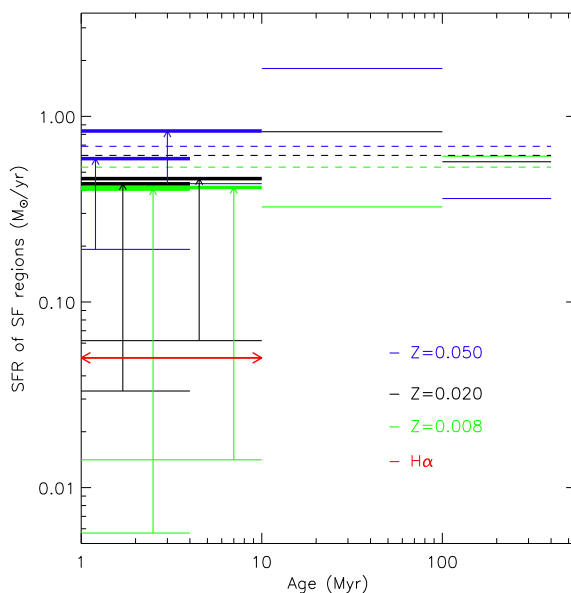
Fig. 14.— SFRs at recent epochs in M31, from our SF regions. Black lines are values derived for solar metallicity, blue lines are for Z=0.05, and green lines are for Z=0.008. In all cases MW-type dust was assumed to correct the UV luminosities for interstellar extinction, as discussed in Section 6. Solid horizontal lines represent the SFR in four time bins: <4, <10, 10-100, and 100-400 Myrs, and the dashed lines are mean values over the past 400 Myrs. The red line is the SFR from Hα (Massey et al. 2007), shown in the <10 Myrs age bin which traces only the youngest stars capable of ionizing the ISM. The thick horizontal lines above vertical arrows on the <4 Myrs age bin and <10 Myrs indicate the total SFRs obtained by adding the SFR from IR measurements (Barmby et al. 2006) to our UV-based estimates.

Table 1.   Details of the selected *GALEX* fields of M31's disk region

No	Field Name	R.A. [deg]	Dec. [deg]	Exp. time [s]	Adopted thresh. [c/s]	Detected pixels above thresh.
1	NGA_M31_MOS11	12.204914	42.956084	3340.35	0.00397	5533
2	NGA_M31_MOS8	12.164794	42.030947	2702.75	0.00384	36791
3	NGA_M31_MOS18	11.403102	42.370208	3244.45	0.00365	77217
4	NGA_M31_MOS4	11.253077	41.863775	3589.70	0.00373	209395
5	PS_M31_MOS00	10.683594	41.277741	3760.10	0.00353	188512
6	NGA_M31_MOS0	10.173990	40.836523	6811.30	0.00324	188847
7	PS_M31_MOS03	9.957439	40.358496	1182.20	0.00446	152669

Table 2.   The UV detected SF regions in M31.[a]

Id	R.A.$_{J2000}$ [deg]	Dec.$_{J2000}$ [deg]	FUV [ABmag]	FUV$_{err}$ [ABmag]	NUV [ABmag]	NUV$_{err}$ [ABmag]	$E(B-V)$ [mag]	Area [arcsec^2]	Age^{b,c} [Myrs]	Age$_{min/max}$^{b,c} [Myrs]/[Myrs]	Mass^{b,c} [M$_\odot$]	Mass$_{min/max}$^{b,c} [M$_\odot$]/[M$_\odot$]	Age^{b,d} [Myrs]	Age$_{min/max}$^{b,d} [Myrs]/[Myrs]	Mass^{b,d} [M$_\odot$]	Mass$_{min/max}$^{b,d} [M$_\odot$]/[M$_\odot$]
1003	12.013985	42.690975	18.870	0.020	19.158	0.013	0.20	112.5	1.6	1.3/ 1.9	3.7e+02	4.4e+02/ 3.7e+02	-99.0	-99.0/ 1.2	-9.9e+01	-9.9e+01/ 3.8e+02
2040	11.951906	42.073174	19.124	0.025	19.331	0.016	0.06	126.0	4.1	2.9/ 5.7	1.4e+02	9.0e+01/ 2.2e+02	2.3	1.8/ 2.7	8.2e+01	8.2e+01/ 1.1e+02
3069	11.725769	41.968216	19.770	0.034	19.986	0.023	0.05	155.2	3.7	2.1/ 5.8	6.8e+01	5.4e+01/ 1.1e+02	2.1	1.4/ 2.7	4.2e+01	5.6e+01/ 5.6e+01
3071	11.715304	41.971684	18.494	0.018	18.420	0.010	0.13	328.5	58.7	49.9/ 66.5	1.5e+04	1.2e+04/ 1.9e+04	22.4	17.6/ 30.8	5.0e+03	5.0e+03/ 8.2e+03
3074	11.641906	41.971554	20.070	0.039	20.057	0.023	0.19	117.0	40.5	24.5/ 49.7	3.2e+03	1.4e+03/ 4.4e+03	10.1	6.8/ 17.5	7.4e+02	4.5e+02/ 1.8e+03
3077	11.618323	41.983509	18.498	0.019	18.633	0.012	0.30	452.2	7.1	5.7/ 8.8	3.3e+03	2.5e+03/ 4.9e+03	3.1	2.8/ 3.6	1.2e+03	1.2e+03/ 1.8e+03
3081	11.635375	41.991177	16.531	0.007	16.393	0.004	0.19	2072.2	79.4	76.8/ 82.0	2.2e+05	2.2e+05/ 2.2e+05	48.0	45.3/ 50.4	1.6e+05	1.6e+05/ 1.6e+05
3082	11.658252	41.985649	18.267	0.016	18.131	0.008	0.26	229.5	74.8	68.9/ 80.6	6.4e+04	6.4e+04/ 7.6e+04	43.3	34.6/ 49.3	4.2e+04	2.8e+04/ 5.6e+04
3083	11.625877	41.988590	19.501	0.032	19.476	0.019	0.46	207.0	19.9	14.8/ 29.8	1.8e+04	7.8e+03/ 3.0e+04	6.2	4.8/ 8.1	4.0e+03	2.6e+03/ 6.8e+03
3085	11.648593	41.992626	20.509	0.055	20.507	0.033	0.30	112.5	28.4	15.2/ 47.0	3.6e+03	2.2e+03/ 6.8e+03	7.7	4.8/ 15.5	8.1e+02	3.1e+02/ 2.7e+03
3086	11.654299	41.999249	17.305	0.011	17.136	0.006	0.20	1055.2	89.3	85.2/ 94.1	1.4e+05	1.4e+05/ 1.4e+05	54.9	52.2/ 57.6	8.9e+04	8.9e+04/ 1.2e+05
...	...	...	...	...	...	...	...	...	...	.../...	...	.../...	...	.../...	...	.../...

[a] Full catalog available in electronic version.

[b] "-99.0" and "-9.9e+01" indicate the cases where the observed color is outside the range of model colors at all ages.

[c] Metallicity Z=0.02 and average MW ($R_V = 3.1$) dust type.

[d] Metallicity Z=0.05 and average MW ($R_V = 3.1$) dust type.

Table 3.   M31 SFR derived from UV flux in different age intervals.

Metallicity	SFR[$M_\odot$/yr] from UV-detected SF regions				
(Z)	<4 Myrs*	<10 Myrs*	10-100 Myrs	100-400 Myrs	<400 Myrs
0.008	0.006(0.406)	0.014(0.414)	0.325	0.610	0.532
0.020	0.033(0.433)	0.062(0.462)	0.826	0.569	0.616
0.050	0.192(0.592)	0.434(0.834)	1.811	0.361	0.690

*The value inside parentheses is obtained by adding the SFR from IR measurements (Barmby et al. 2006) to the SFR derived from our UV measurements.